Invited Paper

Optical couplers for terahertz quantum well photodetectors

R. Zhang, X. G. Guo, and J. C. Cao [*]

Key Laboratory of Terahertz Solid-State Technology, Shanghai Institute of Microsystem and Information Technology,
Chinese Academy of Sciences, Shanghai, 200050, China

[*] Email: jccao@mail.sim.ac.cn

Abstract: Constrained by the intersubband transition selection rule, terahertz (THz) quantum well photodetectors (QWPs) are insensitive to the normally incident light. On the other hand, the intersubband absorption efficiency of THz QWPs is relatively low due to the low doping concentrations in the quantum wells. To solve these issues, optical couplers including the metal-grating coupler, the micro-cavity coupler, and the surface-plasmon coupler, are introduced and investigated. Our findings show that, with these high efficient optical couplers, the performance of THz QWPs can be greatly improved.

1. Introduction

Terahertz (THz) quantum well photodetectors (QWPs) have been demonstrated to be fast, compact, and high efficient THz photon detectors [1-3]. The device structure is simple, and the material (GaAs/AlGaAs) growth and device fabrication techniques are well developed, which makes it possible to construct large-scale uniform focal plane arrays. Due to these merits, THz QWPs are considered potential candidates for various THz applications [4-8], such as high-speed THz communication, real-time THz imaging, medical diagnosis, etc.

THz QWPs are developed from quantum well infrared photodetectors (QWIPs), which was firstly demonstrated by Liu et al in 2004 [1]. Similar to QWIPs, the mechanism of THz QWPs is also based on the intersubband transitions (ISBT) of electrons in the conduction band. The ISBT selection rule requires a non-zero polarization component in the epitaxial growth direction [9], which means THz QWPs are insensitive to the normally incident light. In practical measurements, configurations of 45º-facet incidence and Brewster-angle incidence are commonly used [10], as illustrated in Fig. 1. Although these methods are simple, and are also proved to be effective, both of them are not suitable for the construction of focal plane arrays where normal incidence is required. Also, in both configurations, only part of the p-polarized incidence can contribute to the

ISBT, leading to a relative low coupling efficiency. Another important limitation in THz QWPs is the low doping concentration in the quantum wells. Although the dark current is reduced at low doping levels, the intersubband absorption efficiency also decreases. Also, it has been proved that the absorption efficiency cannot be improved by simply increasing the doping due to the many-body interactions [11]. To solve the above problems and improve the device responsivity, optical couplers are utilized and investigated in this paper.
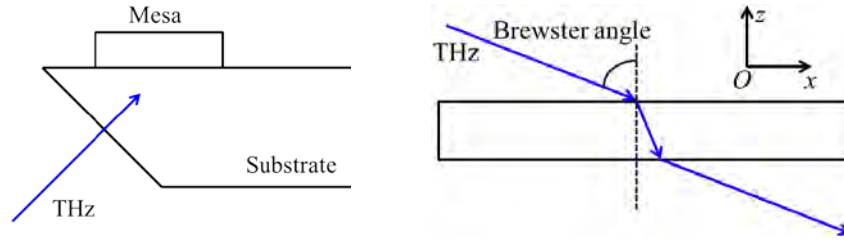

Fig. 1 Commonly used coupling geometries. Left: 45°-facet incidence; Right: Brewster-angle incidence. E_z is the polarization required by ISBT. Inset: the coordinate system used in this paper.

Optical couplers [12-18] are expected to not only change the polarization of the incident light, but also improve the coupling efficiency. In the following, a 1-dimentional (1D) grating coupler is introduced firstly. The coupling efficiency is carefully investigated theoretically and experimentally. Our findings show that such simple coupler could solve the normal-incidence problem and provide a comparable coupling efficiency with the facet device. Based on the study of 1D metal-grating coupler, the micro-cavity coupler and the surface-plasmon-polariton (SPP) coupler are proposed. Significant improvements are found in the simulated results by the finite element method (FEM). At last, the zone-plate coupler is briefly discussed.

2. 1D grating coupler

Gratings are widely used as couplers for QWIPs [19]. In the following, 1D grating coupler will be employed for THz QWPs. Both transmission grating and reflection grating will be investigated. The commercial finite element method software COMSOL is used to simulate the coupling efficiency of the 1D grating. The coupling efficiency is expressed by the average intensity ($I_{average}$) of E_z component in the active region (Volume: V_{AR}).

$$I_{average} \propto \frac{\int_{V_{AR}} |E_z|^2 \, dV}{V_{AR}}. \tag{1}$$

The material parameters used in all the simulations in this paper are given as follows. The permittivity of GaAs is given by [20]

$$\varepsilon(\omega) = \frac{\omega_{TO}^2 (\varepsilon_s - \varepsilon_\infty)}{\omega_{TO}^2 - \omega^2 - i\omega\delta_{TO}} + \varepsilon_\infty \left[1 - \frac{\omega_P^2}{\omega(\omega + i\delta_P)} \right], \tag{2}$$

where $\varepsilon_s = 12.85$, $\varepsilon_\infty = 10.88$, $\omega_{TO} = 2\pi \times 8.02 \text{ THz}$ and $\delta_{TO} = 2\pi \times 0.06 \text{ THz}$. δ_P is the damping rate depending on the doping density N_P. ω_P is the plasma frequency.

$$\omega_P = \sqrt{\frac{N_P e^2}{\varepsilon_0 \varepsilon_\infty m^*}}, \tag{3}$$

where e is the elementary charge, ε_0 is the vacuum permittivity, and m^* is the effective mass of electron.

The permittivity of metal is given by

$$\varepsilon_M(\omega) = 1 - \frac{\omega_M^2}{\omega(\omega + i\delta_M)}, \tag{4}$$

In the case of gold, we have $\omega_M = 1.11 \times 10^4 \text{ THz}$ and $\delta_M = 83.3 \text{ ps}^{-1}$.

2.1. Transmission grating

As illustrated in Fig. 2, the grating metal is defined on the top of the device mesa by standard GaAs processing techniques. The grating material is Ti/Pt/Au (25/55/300 *nm*). The THz QWP studied here is labeled as V266, and the structure parameters are given in [2]. The terahertz wave is normal incident onto the grating, and all the diffraction modes except the 0th diffraction one will contribute to the intersubband transitions.
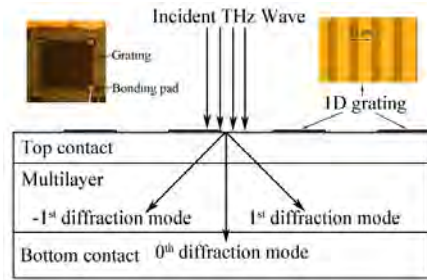

Fig. 2 Schematic of transmission-grating-coupled THz QWP. The multilayer is the active region. Insets: (left) top view of the mesa and (right) microscope picture of the grating. [13]

The dependence of $I_{average}$ and the grating parameters are systematically simulated in [14]. The results show that for an optimum grating, the period (p) (cutoff wavelength) should be equal to the peak response wavelength in the device material (λ_P/n_r). The intrinsic photocurrent response of V266 is obtained by measuring the 45º-facet device. As shown in Fig. 3(a), the peak response frequency is ~5.4 *THz*, corresponding to the wavelength of ~14.6 *μm* in GaAs. To verify the simulation results, 3 grating-coupled THz QWPs with different grating periods are fabricated, which are labeled as V266-G12 (12-*μm*-period grating), V266-G15 (15-*μm*-period grating), and V266-G20 (20-*μm*-period grating) respectively. The measured photocurrent spectra and responsivities are given in Fig. 3. The vertical lines indicate the grating positions (the period/cutoff of the grating). As the prediction, the peak responsivity of V266-G15 is the highest, where the grating period is the closest to λ_P/n_r (n_r is the refractive index of GaAs). The distortion of the spectrum of V266-G12 at ~6.3 *THz* is also due to the maximum coupling efficiency at the grating position. It is worth noting that, below the cutoff frequency, all the diffraction modes expect the 0th mode become evanescent waves which propagate along the grating/semiconductor interface. This confirms that evanescent waves can also contribute to the ISBT and be detected by THz QWPs.
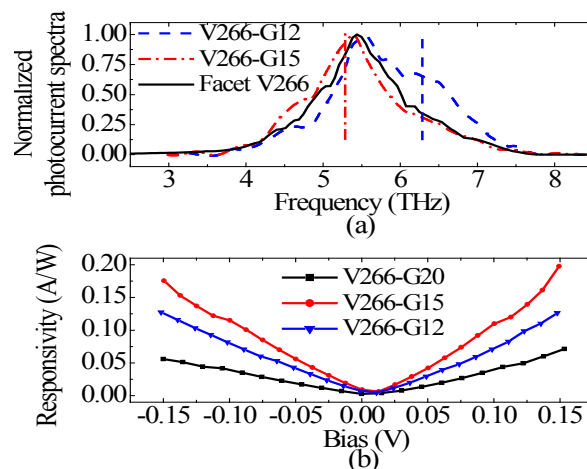

Fig. 3 (a) Normalized photocurrent spectra of V266-G12 (blue dashed line) and V266-G15 (red dash-dotted line), and the one of facet sample (black line) is also given for comparison. The vertical lines indicate the cutoff of two gratings: the blue one corresponds to 12-*μm*-period grating, and the red is for 15-*μm*-period grating; (b) Peak responsivities of V266-G12, V266-G15, and V266-G20. [13]

From the above analysis, it is seen that, for the 1D transmission metal-grating coupler, (a) the operation at the normal incidence is realized; (b) the optimum grating period should be equal to the peak response wavelength; (c) the near field plays an important role in the coupling; and (d) as will be shown in the following, the performances of grating-coupled device and the 45º-facet one are comparable.

Recently, several THz QWPs have been fabricated to directly compare the performances of the grating device and the facet device [15]. The peak response frequency is ~5.85 *THz*. The

characterizations include the measurements of the background limited infrared performance (BLIP) temperature, the photocurrent spectrum, and the responsivity. The results are given in Fig. 4 & 5. It is seen that the BLIP temperature T_{BLIP} of the grating-coupled device is slightly higher. At the T_{BLIP}, the photocurrent is equal to the dark current. Higher T_{BLIP} means higher dark current, and therefore, higher photocurrent. That is to say, under the same background illumination, the photocurrent of the grating-coupled device is higher than that of the facet device, indicating a better coupling efficiency of the grating-coupled device. This is also confirmed by the responsivity measurements, which are shown in Fig. 5. Note that the photocurrent spectra of both devices are similar because the grating position is near the peak response wavelength, and the oscillations in Fig. 5(a) are caused by the Fabre-Perot cavity which is actually the substrate [21]. The oscillations are obvious in the grating-coupled device because the light is normal incident.
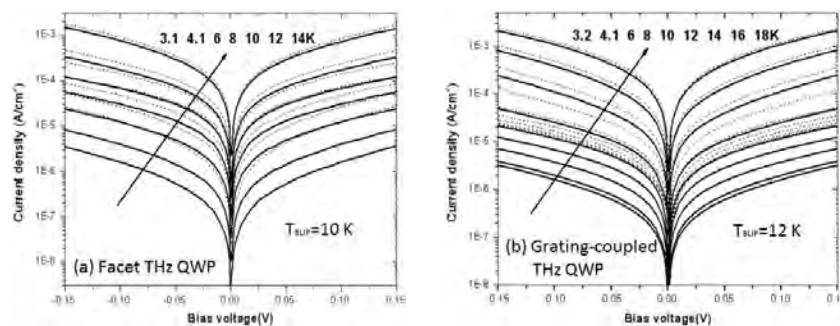

Fig. 4 BLIP temperature measurements. (a) facet THz QWP; (b) grating-coupled THz QWP. [15]
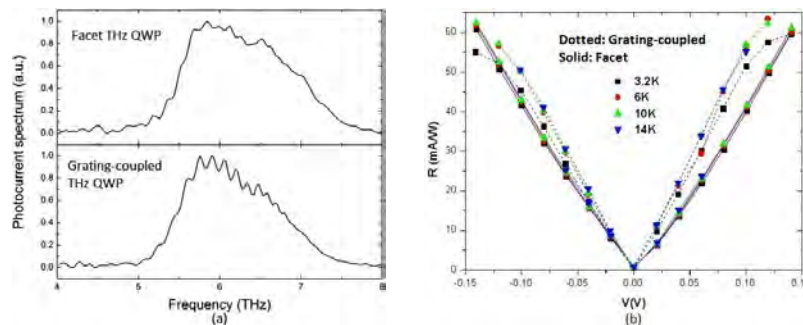

Fig. 5 (a) Photocurrent spectra of facet THz QWP (Top) and grating-coupled THz QWP (bottom); (b) Responsivity of facet THz QWP (solid) and grating-coupled THz QWP (dotted). [15]

2.2. Reflection grating

For reflection gratings [16], the THz waves are incident from the back side of the device, and the diffractions at the reflective side are used for the light coupling, as shown in Fig. 6. The periodic grooves on the top contact are completely coated with gold to form the reflection grating. Assume the peak response frequency of the THz QWP is ~4.05 *THz*, according to the results in Sec. 2.1, the grating period *p* should be 20 *μm*. Based on simple optics arguments, the grating

height h should be $\lambda_p/4n_r$ to eliminate the 0th diffraction mode due to the destructive interference. Here, the relation between the coupling efficiency and the grating height is shown in Fig. 7. The wavelength in the device material is $\lambda_p/n_r = 20\,\mu m$, hence, $\lambda_p/4n_r$ gives a height of 5 μm; while in Figure 7, the best height is 1.4 μm. A significant difference is found between the simple optics arguments and the simulations.
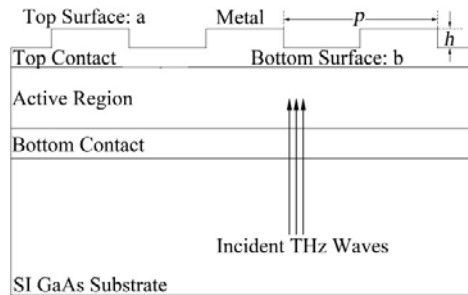

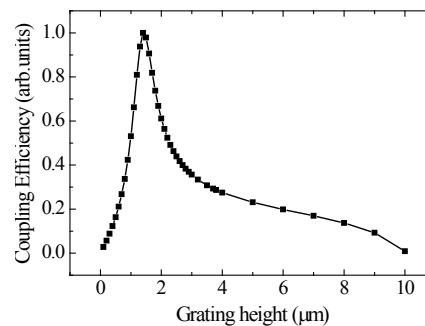Fig. 6 Schematic of the reflection-grating-coupled THz QWP. [16]

Fig. 7 Coupling efficiency (normalized) at different grating heights. The grating parameters are *p*=20 *μm*, fill factor
     r=50%, and the incident frequency is *f*=4.05 *THz*. [16]

To analyze the above differences, the coupling efficiency at different frequencies are investigated and shown in Fig. 8. It is seen that, at small etch depths, the behavior of the grating is similar to the results in [14]. However, as the etch depth becomes larger, new characteristics appear, such as new peaks (A1, A2…, defined as A-peak here) and a new valley (B). These characteristics could be attributed to the standing-wave effect in the grating strips. To help understand such standing-wave effect, the electric field distributions of A4 and B in the device are given in Fig. 9. It is known that a standing wave will form when a plane wave is reflected by the metal. At the position $\lambda/4$ away from the metal, it is a maximum (in the intensity of the standing wave); and at the position $\lambda/2$ away from the metal, it is a minimum. As plotted in Fig. 9, A4 actually corresponds to the former case, while B corresponds to the latter. Suppose all the A-peaks follows this rule, an effective refractive index n_{eff} could be extracted, which is given in Fig. 8(b). Now, it is not surprising that there is a deviation between the simple optics arguments and the FEM simulations. Actually, the grating strip and the metal form a coupled system, especially when the grating height is small. The coupled system exhibits a high effective index. It

decouples gradually as the grating height increases, and n_{eff} approaches to the bulk GaAs value asymptotically. Therefore, by introducing the coupled system and n_{eff}, the simple optics arguments are in good agreement with the results of FEM simulations. The optimum grating height is $\lambda_p/4n_{eff}$.

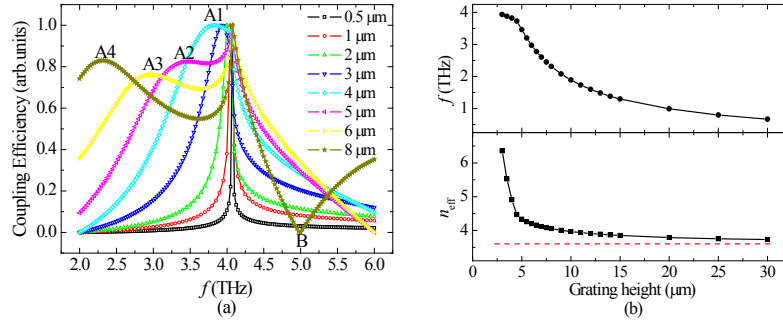Fig. 8 (a) Coupling efficiency (normalized) versus frequency at different grating heights. (b) Frequencies (top) of A-peaks and n_{eff} (bottom) at various etch depths (grating heights). The red dashed line indicates the refractive index of GaAs. [16]
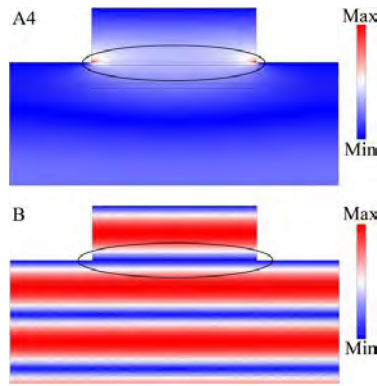

Fig. 9 $|E_x|$ patterns (one period) of A4 (top) and B (bottom) in Fig. 8. The intensity in the region marked by the ellipse determines the near field $|E_z|$. [16]

3. Micro-cavity coupler

Recently, sub-wavelength micro-cavities have been used to confine the light field and investigate the strong interactions between the light and the ISBT [22]. Here, the micro-cavity is used to enhance the electric field in the active region of THz QWPs and improve the coupling efficiency [17]. The micro-cavity coupler is schemed in Fig. 10. The difference between the micro-cavity coupler and the previous grating coupler is that a metal layer is inserted below the bottom contact.
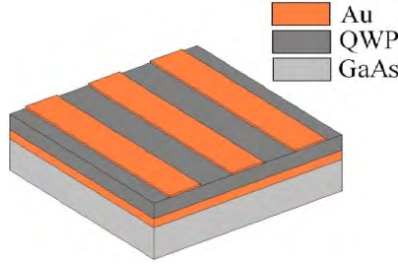
Fig. 10 Schematic of the micro-cavity-coupled THz QWP. [17]

The simulated coupling efficiency of the micro-cavity coupler is shown in Fig. 11. It is seen that the resonant frequency is quite different from the one of the grating coupler. For the same grating parameters, the original coupling peak at ~5.5 *THz* disappears, while two new resonances occur at ~3.6 *THz* and ~7.2 *THz* [Fig. 11(b)]. By using the ray propagation method, it is found the resonant frequency could be fitted by

$$f_{res} = \frac{c}{\sqrt{\varepsilon}} \sqrt{\frac{\left[(2m-1)-\varphi\right]^2}{16L^2} + \left(\frac{n}{p}\right)^2} , \tag{5}$$

where *L* is the cavity height, *p* is the grating period, and φ is the phase shift from the reflection at the grating surface. *m* and *n* are integers. The two terms accounts for the contribution of propagation modes in the cavity and the diffraction modes of the grating respectively. By choosing the proper parameters, the resonance can happen at desired frequencies [Fig. 11(c)], and the coupling efficiency could be improved by two orders of magnitude.
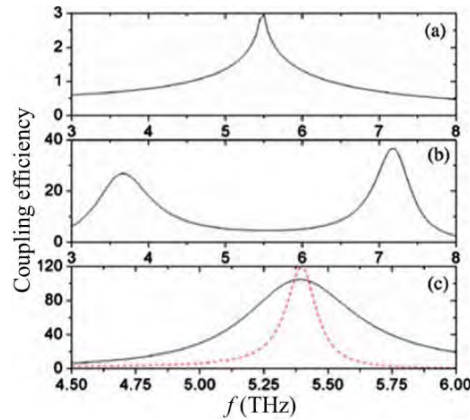

Fig. 11 Coupling efficiency of (a) metal grating coupler. *p*=16.8 *μm*, the width of metal strip is 8.4 *μm*; (b) micro-cavity coupler. The grating parameters are the same as (a). The height of the cavity is *L*=3.8 *μm*; (c) micro-cavity coupler. *p*=20 *μm*. Solid line: metal strip: 6.5 *μm*, cavity height: 2.0; Dashed line: metal strip: 8.0 *μm*, cavity height: 6.0 *μm*. [17]

4. Surface-plasmon-polariton coupler

It is shown in Sec. 2.1 that the surface mode can contribute to the ISBT, and it plays an important role in the light coupling especially when the frequency is below the cutoff frequency of the grating. Therefore, the surface plasmon polariton (SPP) could be considered to enhance the near field and improve the coupling efficiency. The SPPs excited at the metal/semiconductor interface have already been used in the light coupling for detectors in the near infrared region. However, the plasma frequencies of commonly used metals are in the near-infrared, visible, or ultraviolet region. In THz region, these metals behave like perfect conductors. Surface plasmons can hardly be excited on these metal surfaces. An effective alternative is to adopt the doped semiconductor, where the plasma frequency is related to the doping concentration [refer to Eq. (3)], and this method is employed to realize the light coupling in THz QWPs [18]. The SPP-coupled THz QWP is schemed in Fig. 12.
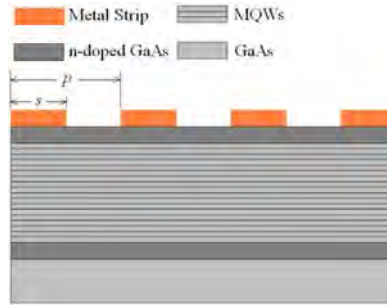

Fig. 12 The schematic of the SPP-coupled THz QWP. Different from the grating-coupled THz QWP, the top contact layer is doped to certain values to have proper plasma frequencies. [18]

The SPP is expected to be excited at the surface of the top contact layer (TCL). The additional wave vector of the SPP is provided by the grating. The field distribution and the dispersion relation in the QWP system are given in Fig. 13. It is seen that there are two kinds of modes. The modes in Fig. 13(b) are the SPP modes supported by the doped-GaAs(TCL)/undoped-GaAs(MQWs) bi-layer system; while the modes in Fig. 13(a) are the modes of the tri-layer system which is illustrated in the inset of Fig. 13 (c). The tri-layer is the air/doped-GaAs(TCL)/undoped-GaAs(MQWs). The dispersion of the tri-layer system is expressed by [23]

$$e^{-4k_1a} = \frac{k_1/\varepsilon_1 + k_2/\varepsilon_2}{k_1/\varepsilon_1 - k_2/\varepsilon_2} \cdot \frac{k_1/\varepsilon_1 + k_3/\varepsilon_3}{k_1/\varepsilon_1 - k_3/\varepsilon_3}, \tag{6}$$

where $k_i^2 = \beta^2 - \varepsilon_i k_0^2$, and ε_i is the permittivity of each layer. The analytical results of this equation are shown in Fig. 13(c), which are in good agreement with those from the FEM simulations. The coupling efficiency is compared with that of the facet device in Fig. 14. The resonant wave vectors are related to the grating period p and the metal strip width s by

$\pm 2\pi m/(p-s)$ for the modes shown in Fig. 13(a). With a proper design, the coupling efficiency could be improved by 30 *times*.
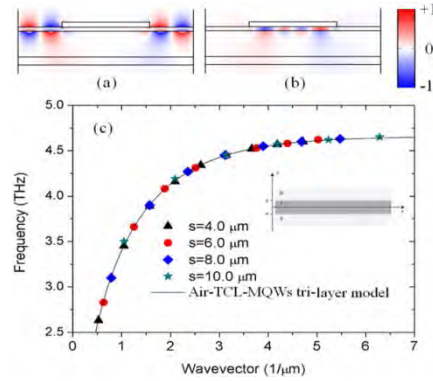

Fig. 13 Electric field distributions of the SPPs. (a) Modes of the tri-layer system; (b) modes of the bi-layer system, and (c) For the tri-layer system, numerical (symbols) and analytical (solid line) results of the dispersion relations of SPPs with different widths of the metal strips. The numerical results are extracted from the field distributions from the FEM simulations. The analytical results are given by Eq. (6). The Si doping concentration is $5 \times 10^{17}/cm^3$ in the 0.4-μm-thick TCL. [18]
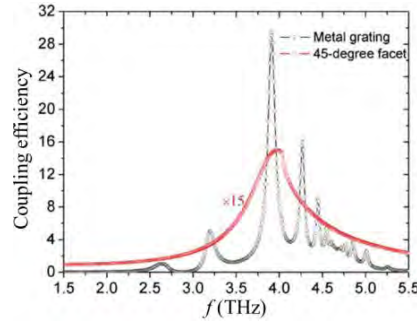

Fig. 14 The coupling efficiencies of SPP-coupled and facet THz QWPs. For clarity, the values of the facet device are multiplied by a factor of 15. [18]

It is worth noting that the SPPs are generated on the doped semiconductor. While recently, the surface modes supported by the subwavelength-structured surfaces are very attractive [24]. Such structured surfaces, i.e. plasmonic metamaterials, can be easily implemented in THz range by designing the structural parameters, and thus can be used in the light coupling of THz QWPs. Couplers with functions of wave-guiding and focusing are expected based on the structured surfaces.

5. Zone plate

The substrate lens is a useful tool to focus the light incident from the back side of the device [Fig. 15(a)], which has already been used in the photodiode [25]. It can also be fabricated on the

substrate of THz QWP to focus the THz waves. Alternatively, similar effect can be achieved by the zone plate [Fig. 15(b)], where the focus length is easy to design according to the thickness of the substrate and the wavelength. The radii of the zone plate is expressed by

$$r_n = \sqrt{n\lambda F + \frac{n^2 \lambda^2}{4}}, \qquad (7)$$

where F is the focus, n is an integer, and λ is the wavelength expected to be focused. For F=600 μm and λ/n_r=15 μm, a focal point is seen at the depth of 600 μm in the electric field distribution shown in Fig. 16(a). Therefore, if a grating-coupled device mesa is fabricated at the focal point as shown in Fig. 16(b), the intensity in the active region should be greatly improved.
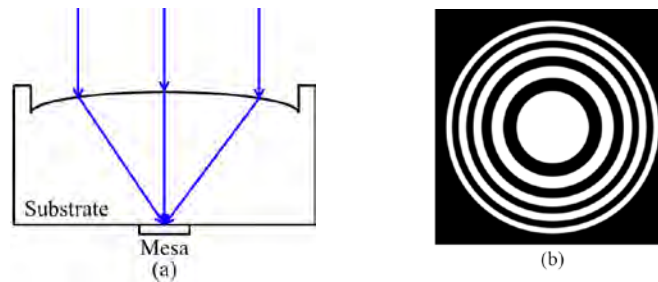

Fig. 15 The schematics of (a) the substrate lens and (b) the zone plate.
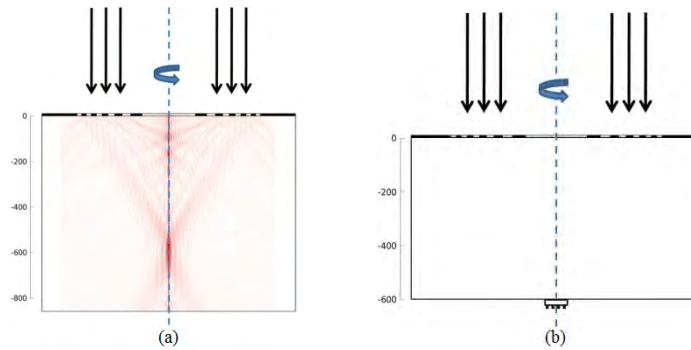

Fig. 16 (a) The distribution of electric field $|E_z|$ in the substrate; (b) The schematic of a THz QWP integrated with a zone plate. The axes on the left give the depth in the substrate.

A particular design of the zone plate is the equally-separated annular grooves which are illustrated in Fig. 17(a). For the parameters given in Fig. 17(b) and f=4.0 *THz*, the distribution of $|E_z|$ is plotted. It is seen that a focus is formed at the center. Actually, by substituting F=0 in Eq. (7), this focus effect can be easily understood. In practice, the low-intensity region can be isolated by proton implant, while high-intensity region at the focus is remained. Then, not only the average intensity in the active region is enhanced, the dark current is also reduced.
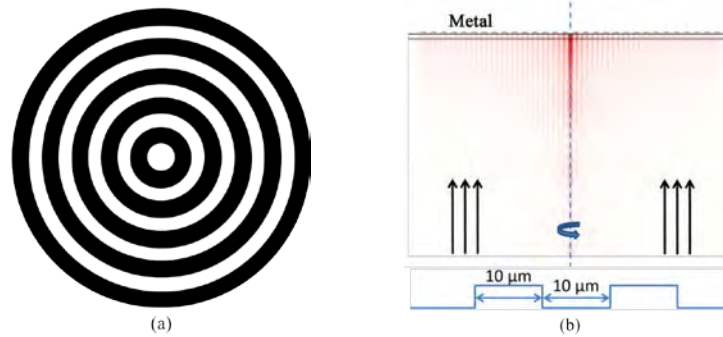
Fig. 17 (a) Schematic of equally-separated annular grooves; (b) Focus effect of the grooves.

6. Conclusions

Since the first demonstration of THz QWP in 2004, tremendous progress has been obtained in the research of THz QWPs. Due to the specific characteristics such as narrow band detection, high speed response, and easy fabrication and integration, THz QWPs are very attractive for diverse application systems. To improve the device performance, recent studies on the couplers for THz QWPs are summarized in this paper. The 1D-grating coupler is simple and effective. The normal incident light is bent by the grating and is successfully detected by the THz QWP. Also, comparable responsivity with the facet device is achieved. To enhance the electric field in the active region, a metal layer is inserted below the bottom contact. Together with the metal grating on the top contact, a metallic micro-cavity coupler is formed. Two resonant peaks are found, which correspond to the waveguide effects and the grating effects respectively. At the resonant frequencies, the coupling efficiency could be improved by two orders of magnitude. It is confirmed that the ISBT can also be excited by the surface modes. Therefore, the SPP coupler, which can enhance the surface modes, is proposed. The SPP modes on the surface of top contact layer are excited by the grating coupler, and 30-*times* enhancement of the electric field intensity is predicted. The zone-plate coupler is also discussed. The zone plate is actually a focus lens. The focusing effect is especially desired in the design of the couplers. The intensity at the focus is strong. Meanwhile, the device area could be shrunk to the focus region, thus, the dark current could be greatly reduced. Consequently, significant increase of the BLIP temperature can be expected. In summary, several optical couplers have been investigated in this paper. With these couplers, operation at normal incidence is realized, and the simulated coupling efficiency is also improved. In the future, we will fabricate and characterize the THz QWPs with these couplers, and investigate structured-surface functional couplers.

References

[1]   H. C. Liu, C. Y. Song, A. J. SpringThorpe, et. al.. "Terahertz quantum-well photodetector". *Appl. Phys. Lett.*, 84, 4068 (2004).

[2]   H. Luo, H. C. Liu, C. Y. Song, et. al.. "Background-limited terahertz quantum-well photodetector". *Appl. Phys. Lett.*, 86, 231103 (2005).

[3]   H. C. Liu, H. Luo, C. Y. Song, et. al.. "Terahertz Quantum Well Photodetectors". *IEEE J. Sel. Top. Quantum Electron.*, 14, 374 (2008).

[4]   P. D. Grant, S. R. Laframboise, R. Dudek, et. al.. "Terahertz free space communications demonstration with quantum cascade laser and quantum well photodetector". *Electron. Lett.*, 45, 952 (2009).

[5]   Z. Chen, Z. Y. Tan, Y. J. Han, et. al.. "Wireless communication demonstration at 4.1 THz using quantum cascade laser and quantum well photodetector". *Electron. Lett.*, 47, 1002 (2011).

[6]   T. Zhou, R. Zhang, X. G. Guo, et. al.. "Terahertz Imaging With Quantum-Well Photodetectors". *IEEE Photon. Technol. Lett.*, 24, 1109 (2012).

[7]   Z. Y. Tan, T. Zhou, J. C. Cao, et. al.. "Terahertz imaging with quantum-cascade laser and quantum-well photodetector". *IEEE Photon. Technol. Lett.*, 25, 1344 (2013).

[8]   X. G. Guo, J. C. Cao, R. Zhang, et. al.. "Recent Progress in Terahertz Quantum-Well Photodetectors". *IEEE J. Sel. Top. Quantum Electron.*, 19, 8500508 (2013).

[9]   H. C. Liu, M. Buchanan, and Z. R. "Wasilewski. How good is the polarization selection rule for intersubband transitions?". *Appl. Phys. Lett.*, 72, 1682 (1998).

[10] H. Schneider and H. C. Liu. "Quantum Well Infrared Photodetectors: Physics and Applications". Berlin, Germany: Springer-Verlag, 13 (2006).

[11] X. G. Guo, Z. Y. Tan, J. C. Cao, et. al.. "Many-body effects on terahertz quantum well detectors". *Appl. Phys. Lett.*, 94, 201101 (2009).

[12] M. Patrashin and I. Hosako. "Terahertz frontside-illuminated quantum-well photodetector". *Opt. Lett.*, 33, 168 (2008).

[13] R. Zhang, X. G. Guo, C. Y. Song, et. al.. "Metal-grating-coupled terahertz quantum-well photodetectors". *IEEE Electron Device Lett.*, 32, 659 (2011).

[14] R. Zhang, X. G. Guo, J. C. Cao, et. al.. "Near field and cavity effects on coupling efficiency of one-dimensional grating for terahertz quantum well photodetectors". *J. Appl. Phys.*, 109, 073110 (2011).

[15] L. L. Gu, X. G. Guo, Z. Y. Tan, et. al.. "Terahertz quantum well photo-detectors: Grating versus 45-degree facet coupling". Unpublished.

[16] R. Zhang, X. G. Guo, and J. C. Cao. "Coupling Efficiency of Lamellar Gratings for Terahertz Quantum-well Photodetectors". *J. Korean Phys. Soc.*, 60, 1233 (2012).

[17] X. G. Guo, R. Zhang, J. C. Cao, et. al.. "Numerical study on metal cavity couplers for terahertz quantum well photodetectors". *IEEE J. Quantum Electron.*, 48, 728 (2012).

[18] X. G. Guo, R. Zhang, J. C. Cao, et. al.. "Surface plasmon-enhanced absorption in metal grating coupled terahertz quantum well photodetectors". *IEEE J. Quantum Electron.*, 48, 1113 (2012).

[19] B. F. Levine. "Quantum-well infrared photodetectors". *J. Appl. Phys.*, 74, R1 (1993).

[20] J. S. Blakemore. "Semiconducting and other major properties of gallium arsenide". *J. Appl. Phys.*, 53, R123 (1982).

[21] R. Zhang, X. G. Guo, J. C. Cao, et. al.. "Asymmetric Fabry-Perot oscillations in metal grating-coupled terahertz quantum well photodetecors". *IEEE J. Quantum Electron.*, 48, 1214 (2012).

[22] Y. Todorov, A. M. Andrews, I. Sagnes, et. al.. "Strong light-matter coupling in subwavelength metal-dielectric microcavities at terahertz frequencies". *Phys. Rev. Lett.*, 102, 186402, (2009).

[23] S. A. Maier. "Plasmonics: Fundamentals and Applications". Berlin, Germany: Springer-Verlag (2007).

[24] J. B. Pendry, L. Martin-Moreno, and F. J. Garcia-Vidal. "Mimicking surface plasmons with structured surfaces". *Science*, 305, 847 (2004).

[25] J. W. Shi, F. M. Kuo, C. J. Wu, et. al.. "Extremely high saturation current-bandwidth product performance of a near-ballistic uni-traveling-carrier photodiode with a flip-chip bonding structure". *IEEE J. Quantum Electron.*, 46, 80 (2010).